Supplementary Material

Title: Virtual stenting with simplex mesh and mechanical contact analysis for real-time planning of thoracic endovascular aortic repair

Authors: Duanduan Chen, Jianyong Wei, Yiming Deng, Huanming Xu, Zhenfeng Li, Haoye Meng, Xiaofeng Han, Yonghao Wang, Jia Wan, Tianyi Yan, Jiang Xiong and Xiaoying Tang

S1. Additional demographic information of the patients

There are sixty-six type-B aortic dissection patients who have experienced thoracic endovascular aortic repair (TEVAR) being included in this study. Among them, stent-graft implantation has been successful in fifty-eight patients, while the eight others have presented distal stent-induced new entry (SINE) as post-TEVAR complications. Additional demographics to supply Table 1 in the main article are listed in the following Table S1.

Table S1. Additional demographics of the included patients.

Diseases	Successfully treated by TEVAR						SINE	P
	cTAG (n=10)	Valiant (n=10)	Zenith (n=10)	Ankura (n=10)	Hercules (n=10)	Grimed (n=8)	- (n=8)	
TBAD duration								
Acute	6	8	8	8	8	7	6	.99
Subacute	4	2	2	2	2	1	2	.84
Chronic	0	0	0	0	0	0	0	.96
Characteristics								
Hypertension	5	6	6	7	4	5	6	.94
Diabetes mellitus	4	3	5	3	3	2	3	.93
Coronary heart disease	0	0	1	0	0	0	2	.44
Arrhythmia	0	0	1	0	0	0	0	.50
Marfan syndrome	0	0	0	0	0	0	0	-
Respiratory sleep apnea syndrome	0	0	0	0	0	0	0	-
Cerebrovascular disease	0	0	0	2	0	0	0	.08
LSA chimney	0	1	3	4	0	0	1	.07
LCCA chimney	0	2	0	0	0	0	0	.07
Stroke	0	0	0	0	0	0	0	-
Proximal SINE	0	0	0	0	0	0	0	-
Distal SINE	0	0	0	0	0	0	8	-
Double SG	9	2	0	1	2	4	0	.08

S2. Imaging acquisitions via CTA and micro-CT scans

CTA datasets were acquired before and after stent-graft implantation via a dual-source CT scanner (SOMATOM Definition Flash, Siemens, Germany). The CTAs of the aorta

were carried out with an injection of 70-90ml of contrast with 50ml of saline chaser; threshold of 80HU; rotation speed of 500ms; collimation of 64; slice of 1.0mm; pitch of 1.0; voltage of 100kV; and current of 200-350mA.

Structural information of the six types of stent-grafts were extracted via a micro-CT scanner (GE Healthcare Explore Locus, USA). Scanning parameters include: effective pixel size of 0.046mm; exposure time of 400ms; detector bin mode of 2x2; voltage of 80kV; and current of 450μA.

S3. Deformable simplex model

Deformable simplex model has been previously applied in object reconstruction [1] and constrained deformation [2]. For stenting studies, it was used to develop the fast contouring simulations for stenting in cerebral aneurysms [3, 4]. The concept of deformable simplex model is to describe the law of motion for simplex mesh via a second-order partial differential equation for moving a mesh under the effect of internal and external forces [1, 2], as shown in Eq.S1, where P_i is the vertex of mesh, m is the vertex mass, t is time and γ is the damping factor, $F_{int}(P_i)$ is the internal surface force while $F_{ext}(P_i)$ is the external surface force. Central finite difference discretization is used to find a numerical approximation for the solution of Eq.S1. The law of motion is then discretized as Eq.S2. Both $F_{int}(P_i)$ and $F_{ext}(P_i)$ are computed at time t, and α and β are weights that are respectively controlling the internal and external force of P_i. It should be noted that, in Eq.S2, the force items have the dimension of a displacement.

$$m\frac{\partial^2 P_i(x,t)}{\partial t^2} + \gamma\frac{\partial P_i(x,t)}{\partial t} = F_{int}\left(P_i(x,t)\right) + F_{ext}\left(P_i(x,t)\right) \qquad \text{Equ.S1}$$

$$P_i^{t+1} = P_i^t + (1-\gamma)\left(P_i^t - P_i^{t-1}\right) + \alpha F_{int}\left(P_i^t\right) + \beta F_{ext}\left(P_i^t\right) \qquad \text{Equ.S2}$$

The simplex meshes ($S \in \mathbb{R}^3$) of the true lumen and stent-graft models were composed of a vertex set. To solve the motion of simplex meshes, the geometric characteristics of the vertex set need to be understood. As shown in Figure 2E in the main article, each vertex P_i is connected to three neighboring points P_{iN1}, P_{iN2}, and P_{iN3}. In general, these

three points define a tangent plane towards P_i, and the four vertices (P_i, P_{iN1}, P_{iN2}, P_{iN3}) can be circumscribed by a sphere. The simplex angle $\varphi_i = \angle(P_i, P_{iN1}, P_{iN2}, P_{iN3})$ can then be calculated by the spatial vectors of the vertices, the normal vector of to the tangent plane n_i, the radius of the circle defined by the tangent plane r_i as well as the radius of the vertices-defined sphere R_i. It defines the local shape around a given vertex, *i.e.* the extrinsic curvature of the surface. As shown in Figure 2E in the main article, f_i denoting the orthogonal projection of P_i onto the tangent plane can described as Eq.S3, where ω_1, ω_2 and ω_3 are the parameters to describe the relative position of vertex P_i according to its three neighbors. This parameter with the weights indicates the force item of Eq.S2.

$$f_i = \omega_1 P_{iN1} + \omega_2 P_{iN2} + \omega_3 P_{iN3}$$
$$\omega_1 + \omega_2 + \omega_3 = 1$$

Eq.S3

S4. Measurements in compressive radial tests.

As shown in Figure 3A in the main article, along each stent-graft, radial compressive tests and geometric measurements were conducted regionally on the proximal and distal strut rings as well as three rings with repeating pattern in the main body. The detailed geometric measurements are shown in Table S2.

Table S2 Measurements of stent grafts for compressive tests

Stent-grafts	Depth [mm]			Initial diameter [mm]			Radial deformation [mm]		
	P[1]	B[2]	D[1]	P	B	D	P	B	D
cTag	14	11	12	31.60	31.60	31.60	5.28	5.28	5.28
Valiant	19	17	17	34.60	34.83	32.40	5.78	5.82	5.41
Zenith	25	21	24	43.60	42.50	44.20	7.28	7.27	7.38
Ankura	20	15	16	35.70	31.52	25.50	5.96	5.26	4.26
Hercules	33	17	17	42.80	35.07	35.00	7.15	5.86	5.85
Grimed	33	18	18	31.30	28.63	25.40	5.23	4.78	4.25

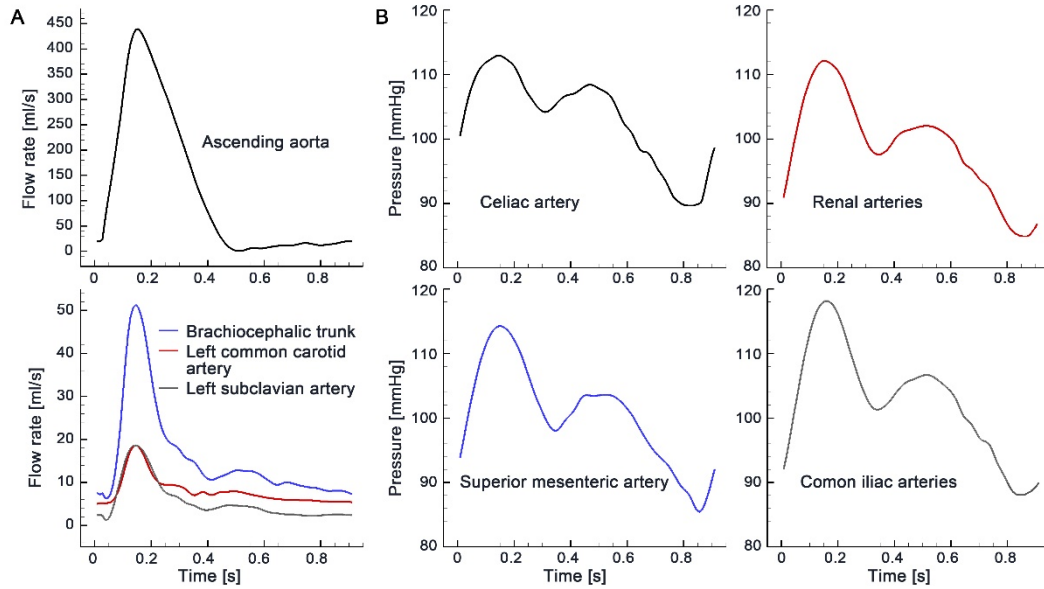[1] – P and D denote the proximal and distal positions of the stent-graft respectively.
[2] – B denotes the positions in the main body of the stent-graft. The values in the B-column are the averaged data of three measurements in this region.

S5. Velocity and pressure boundary conditions

As mentioned in the manuscript, pulsatile velocity boundaries have been assigned to the inlet of ascending aorta and the outlets of aortic arch branches. For each patient, Doppler ultrasound velocimetry was performed. The detailed parameters of the measurement is shown in Table S3. The velocity of ascending aorta was measured through the apical 5-chamber view as well as the suprasternal long axis view of aortic arch. The two results have been compared to each other to ensure the maximum velocity at ascending aorta could be obtained. On the other hand, the velocity at other sites was measured at a proximal and a distal site of the specific vessel (please refer to Table S3 for the detailed positions). The two results of one particular vessel were compared. If the difference was less than 5%, the measurement was considered effective. At each measurement site, appropriate ultrasound probe was employed, the Doppler gate was positioned at the center of the blood vessel, and the Doppler angle cursor was accurately aligned with the vessel axis. The velocity sonogram can then be obtained and the upper edge of it was extracted as the variation of the maximum velocity at each measured site. The flow rates at each velocity boundary can therefore be calculated based on the measured time-variant maximum velocity and the assumed flow profile (flat profile for ascending aorta and parabolic profile for the others). Figure S1A shows the boundary flow curves of a representative case.

Table S3 Parameters of Doppler ultrasound velocimetry

Vessel	Position	View	Doppler angle
Ascending aorta	- 2.5cm above aortic valve	1. Suprasternal long axis view of aortic arch	30
		2. apical 5-chamber view	22
Brachiocephalic trunk	D - 0.8cm below bifurcation	long axis view of the vessel	47
	P - 0.9cm above aortic arch		47
Left common carotid artery	D - 3.0cm below bifurcation	long axis view of the vessel	47
	P - 1.1cm above aortic arch		36
Left subclavian artery	D - 3.0cm above aortic arch	long axis view of the vessel	30
	P - 1.0cm above aortic arch		36

Figure S1 The velocity (A) and pressure (B) boundaries of a patient case. The velocity boundaries were patient-specific while the pressure boundaries were extracted from a previous study.

On the other hand, for the pressure boundaries on the outlets of celiac artery, superior mesenteric artery, renal arteries and common iliac arteries, pulsatile waveforms of pressure were obtained from a previous study [5], as shown in Fig.S1B.
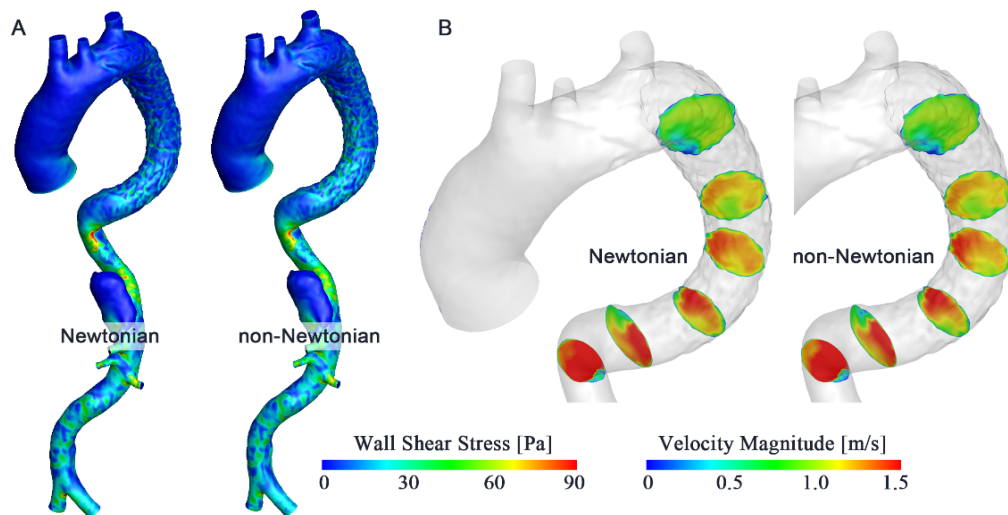
S6. Fluid property study

In the current study, the fluid in the aorta was considered as Newtonian fluid. In fact, non-Newtonian model would provide more accurate simulations of the blood property; however, due to the relatively high shear rate in large arteries and with the consideration of computational load, the blood flow in aorta is often assumed as Newtonian fluid [6-8]. To quantify the difference between the Newtonian and non-Newtonian simulations, one representative case in each stent-graft group was selected to compute in both fluid property models. In the Newtonian model, the density and viscosity of the blood were $1044kg/m^3$ and $0.00365kg·m^{-1}·s^{-1}$, respectively. In the non-Newtonian model, the density of the fluid was the same as the Newtonian model, while, generalized power law was applied for the viscosity, which is described as Eq.S4:

$$\mu = 0.1 \cdot \lambda \cdot \dot{\gamma}^{n-1}$$

$$\lambda = \mu_{\text{inf}} + \Delta\mu \cdot \exp\left[-\left(1 + \frac{\dot{\gamma}}{a}\right) \cdot \exp\left(\frac{-b}{\dot{\gamma}}\right) \right] \qquad \text{Eq.S4}$$

$$n = n_{\text{inf}} - \Delta n \cdot \exp\left[-\left(1 + \frac{\dot{\gamma}}{c}\right) \cdot \exp\left(\frac{-d}{\dot{\gamma}}\right) \right]$$

where, μ_{inf} is 0.035, n_{inf} is 1.0, $\Delta\mu$ is 0.25, Δn is 0.45, and a, b, c, d are respectively assigned as 50, 3, 50 and 4 [9].

As shown in Figure S2, the general distribution patterns and variations of wall shear stress and velocity were compared. In the tested cases, the flow characteristics are exactly the same between the two models of blood property, while, the wall shear stress in the non-Newtonian model is slightly lower. The average difference of the wall shear stress at systolic peak is approximately 10% while the average difference of cross-sectional velocity is about 3%. In the current study, instead of revealing the absolute value of flow quantities, the flow computation was used to compare the difference between the CT-reconstructed and VSA-simulated aortic models. Since the both of the flow models are able to capture flow characteristics, the Newtonian model with less computational expense has been applied in this study.

Figure S2 (A) and (B) show the wall shear stress and velocity distributions respectively based on the Newtonian and non-Newtonian flow models.

S7. Spatial and temporal independency study

To confirm the computational sensitivity to the spatial and temporal resolutions, grid independence analysis and time-step sensitivity test were conducted. The sensitivity study was applied on one aortic model in each stent-graft group, as shown in Figure S3A. The base grids for the six models are listed in Table S4, and the base time-step number per cardiac cycle for all of the models are set to 50. Finer grids of each model were studied (Table S4) and finer temporal resolutions with 100 time steps per cardiac cycle were tested.

Table S4 Grid and time step information and comparison of results

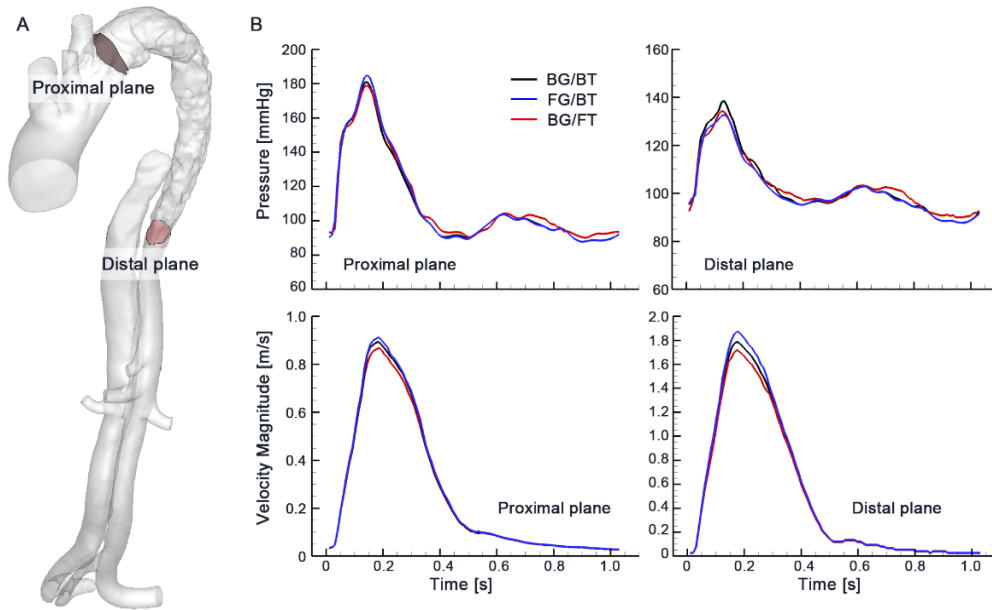| Case	Base grid [cell]	Fine grid [cell]	Pressure difference [%]		Velocity difference [%]	
			Proximal	Distal	Proximal	Distal
Valiant	2,563,411	8,585,277	2.10	2.31	3.12	3.50
Zenith	2,174,160	6,082,448	1.77	1.76	2.75	3.01
cTag	2,100,876	5,617,656	2.33	2.53	3.78	3.88
Hercules	2,712,416	8,323,211	1.89	2.26	2.03	2.37
Ankura	2,206,512	5,932,838	1.97	2.60	2.12	3.00
Grimed	2,297,235	6,671,990	1.68	1.90	2.84	3.11
Case	Base time step [s]	Fine time step [s]	Pressure difference [%]		Velocity difference [%]	
			Distal	Proximal	Distal	Proximal
Valiant	0.0207	0.0103	1.98	2.04	2.55	3.08
Zenith	0.0185	0.0092	1.83	2.34	2.21	2.45
cTag	0.0167	0.0083	1.76	2.05	2.78	2.93
Hercules	0.0200	0.0100	2.13	2.93	2.10	2.67
Ankura	0.0176	0.0088	2.39	2.41	1.99	2.90
Grimed	0.0182	0.0091	2.20	1.72	1.79	2.06

The computational results show highly similarity between the base grid with base temporal resolution model (BG/BT model), base grid with finer temporal resolution model (BG/FT model), and finer grid with base temporal resolution model (FG/BT model). As shown in Figure S3B, at systolic peak, the velocity and wall shear stress

distributions are exactly the same between the three models of each patient case.

To further quantify this, since we focus on the descending aorta, two cross-sectional slices were selected to investigate the velocity and pressure variations. These two aortic cross-sections were selected at the proximal and distal stented region for each patient case. Figure S4 shows one representative case for example. The maximum discrepancies of the velocity magnitude at the proximal and distal planes over a cardiac cycle between the BG/BT and FG/BT models are 5.46% and 5.13%, respectively, while the maximum pressure difference of them are 3.23% and 4.21%. For the BG/BT and BG/FT models, the maximum difference of velocity between the two planes are 4.52% and 5.08% respectively, and the maximum pressure discrepancies are 5.02% and 3.90%,

Figure S3 (A) The models of the patient cases involved in sensitivity tests. (B) The computational results at systolic peak. The velocity streamlines and wall shear stress distributions show exactly the same pattern between the BG/BT, BG/FT and FG/BT models.
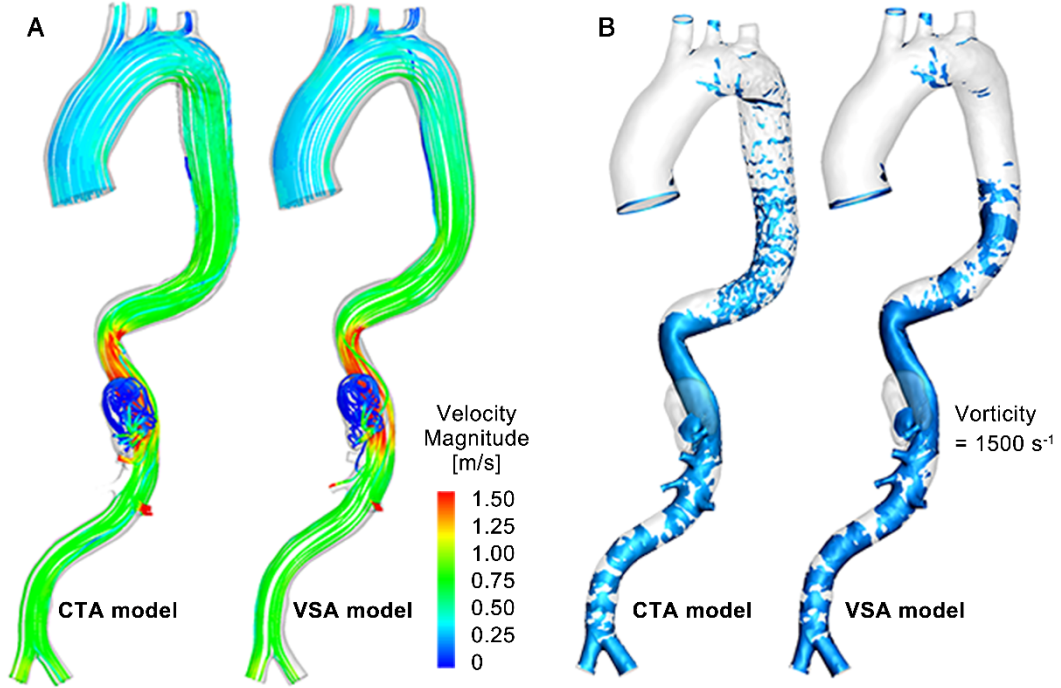
Figure S4 (A) The proximal and distal cross-sectional planes of a representative model. (B) The variations of the average pressure and velocity on these planes. The trends of these variation curves are the same between the BG/BT, BG/FT and FG/BT models, and discrepancies of the velocity and pressure are trivial among the three models.

for the proximal and distal plane respectively. The average discrepancies for pressure and velocity at the two planes for each model are listed in Table S4. Thus, for the purposes of our study, the base resolutions with the base time step are considered adequate.

S8. Additional information of hemodynamic comparisons

Similar flow patterns were found between the CTA model and VSA model. Figure S5 shows the velocity streamlines and vorticity iso-surface (=1500/s) at systolic peak for the CTA and VSA models. The same distribution patterns for both the hemodynamic parameters can be found between the CTA and VSA models.

Time-averaged wall shear stress (TAWSS), oscillatory shear index (OSI) and relative residence time (RRT) between the post-TEVAR CTA model and the simulated VSA model in each patient case were compared. All of the three parameters are derived based
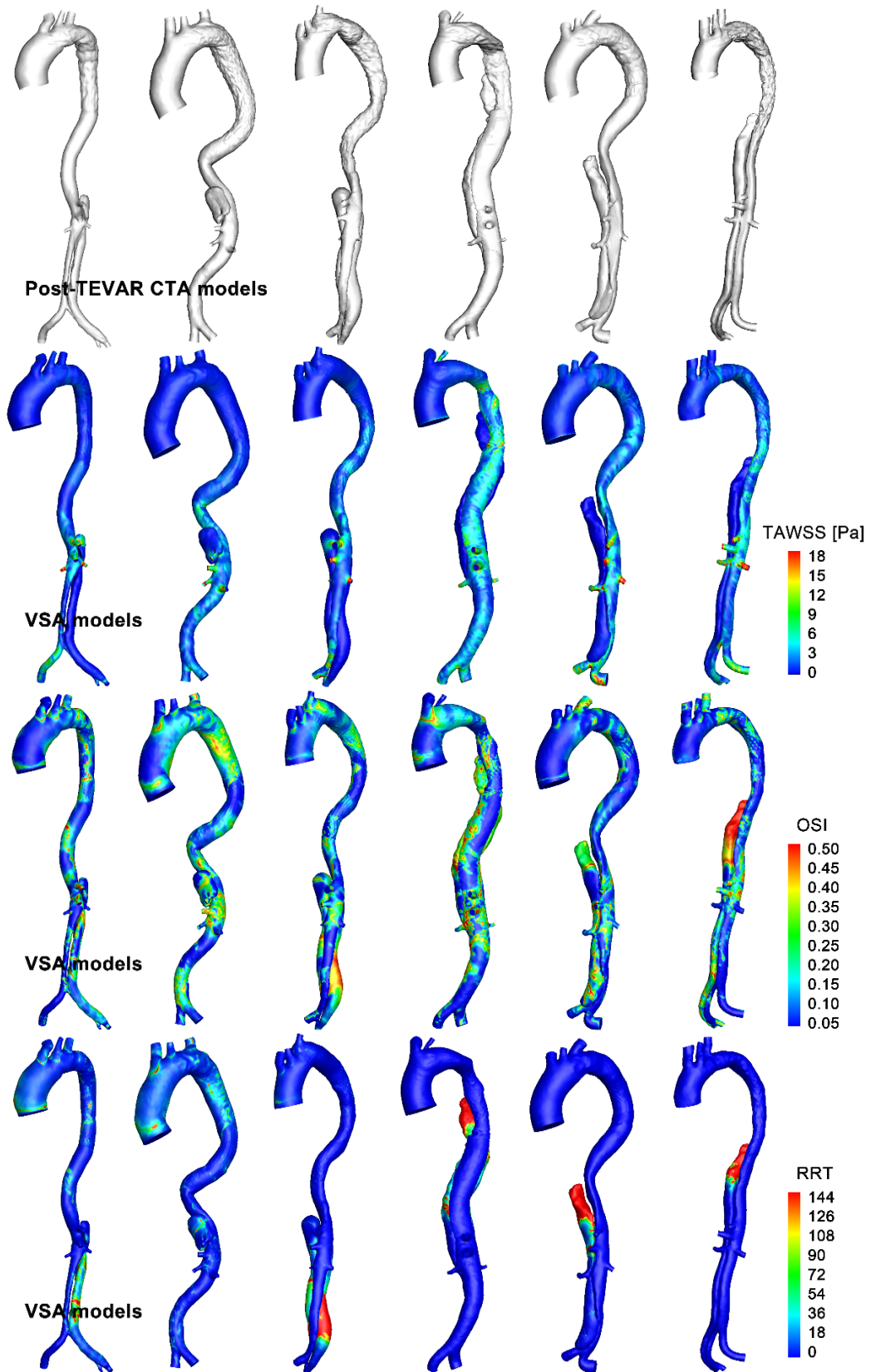
Figure S5 The comparison of velocity streamlines (A) and vorticity iso-surface (B) at systolic peak between the CTA and VSA models.

on wall shear stress and time as Eq.S5. Results of a few cases are shown in Figure 7 in the main article and in Figure S6.

$$\mathrm{AWSS} = \left(\int_0^T |\boldsymbol{WSS}| \, dt \right) / T, \quad OSI = \frac{1}{2} \left(1 - \left(\left| \int_0^T \boldsymbol{WSS} \, dt \right| \right) \middle/ \left(\int_0^T |\boldsymbol{WSS}| \, dt \right) \right)$$

$$\mathrm{RRT} = \left((1 - 2 \cdot \mathrm{OSI}) \cdot \mathrm{AWSS} \right)^{-1} \qquad \text{Eq.S5}$$
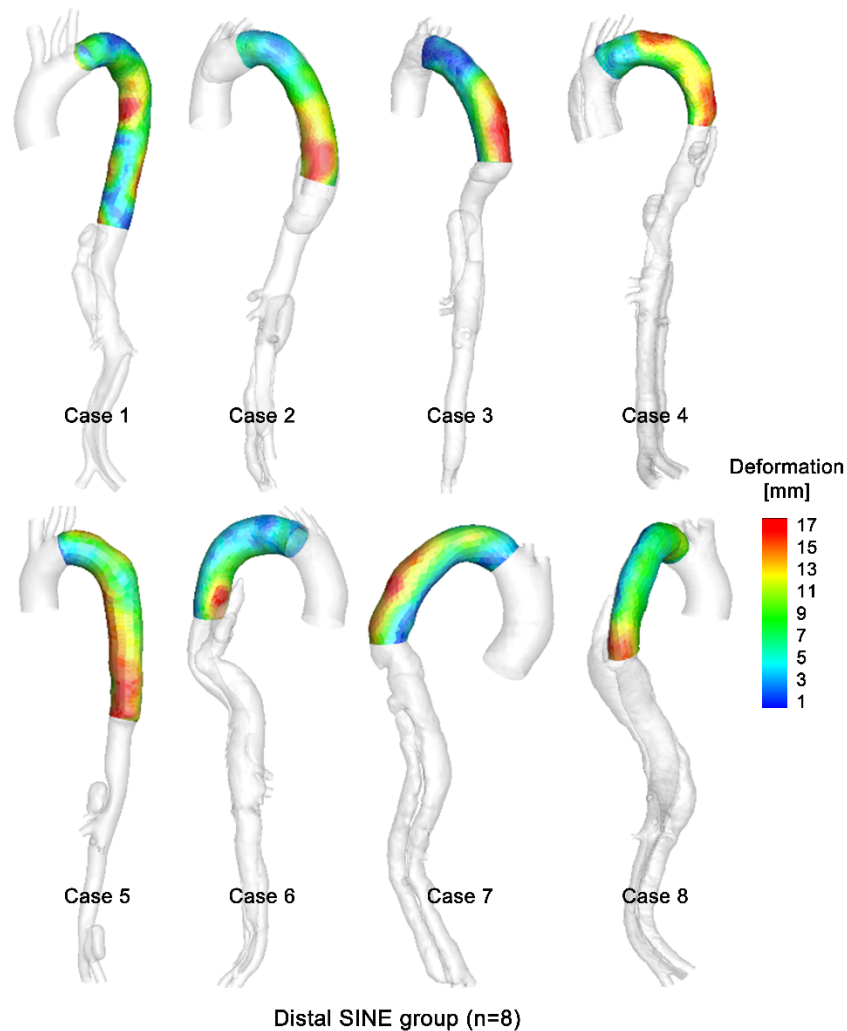
General pattern similarity can be directly observed. Quantified similarity is achieved by the average Hash algorithm via the value matrix as described in the main article (Figure 7D). In brief, the average gray value of each matrix element is calculated. The hash of each matrix based on whether the color value of each element is above or below the mean value can then be constructed. The ratio of the number of the hash values that are different between the two matrixes to the total number is used to evaluate the consistency.

Figure S6 The CTA-reconstructed post-TEVAR models and hemodynamic computational results for one representative patient case in each stent-graft group.

S9. Distribution of stent-induced vessel deformation in all of the studied cases

The proposed VSA facilitates us to analyze the stent-induced vessel wall deformation quantitatively. Figure S7 shows the results for the patients with distal SINE. High deformation region can be identified. Figure S8 shows the deformation results for all of the fifty-eight successfully treated patients. With more cases with post-TEVAR complications being included in the future study. Specific deformation criteria for different complications can be determined, thus to assist quantitative evaluation of treatment risks.

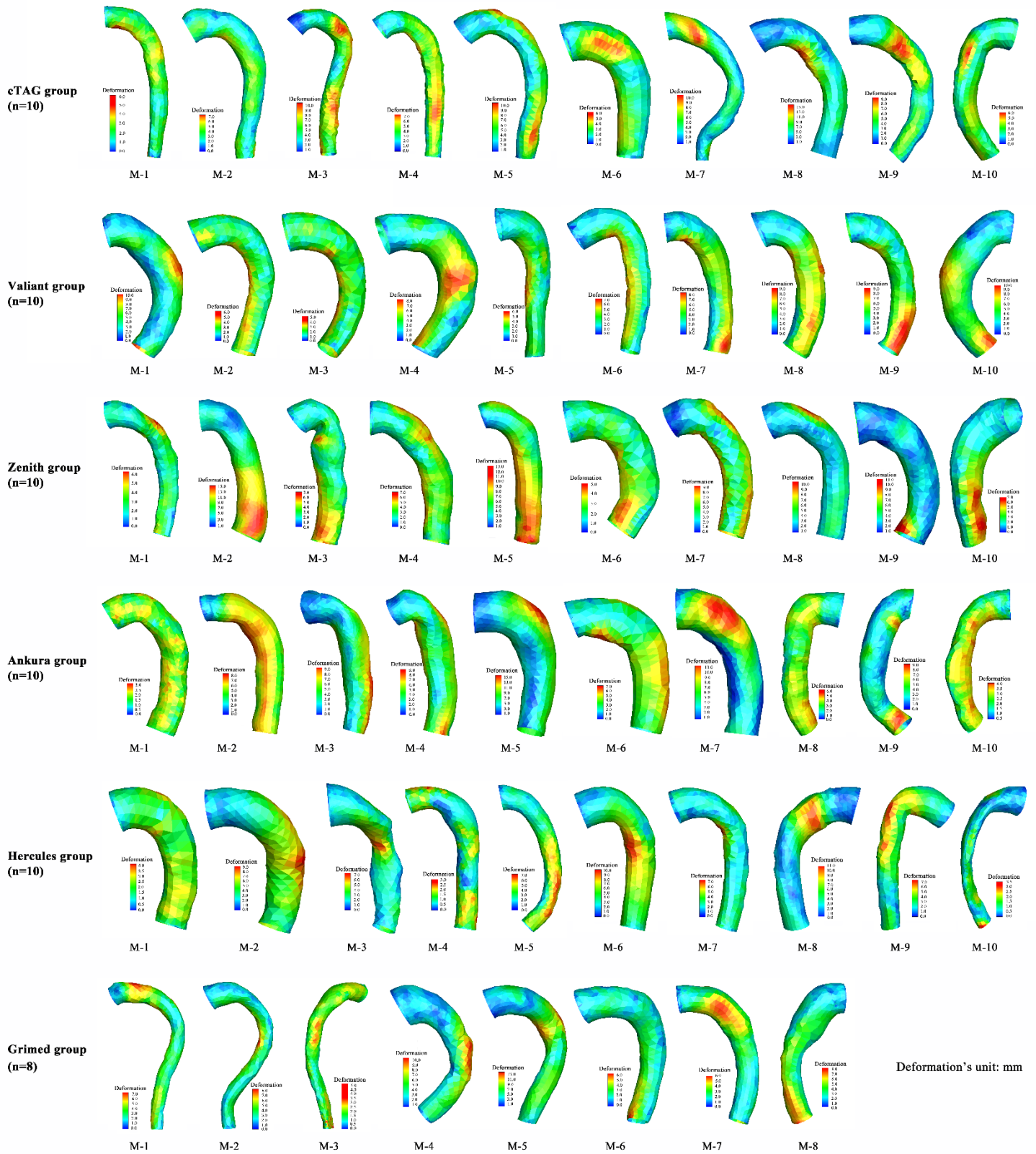**Figure S7** Stent-induced vessel wall deformation of the eight distal SINE cases.

Figure S8 Stent-induced vessel wall deformation of the six stent-graft groups.

S10. Statistical data of stent-induced vessel deformation

Averaged stent-induced deformation has been calculated along the three segments of aorta, along the convex and concave, and along the tear-side curve and opposite curve (detailed measurement methods please refer to the main article). Data extraction and calculation are shown in the Table S5, where statistical analysis was applied among stent-graft groups and between the successfully treated cases and those with distal stent-induced new entry.

Table S5 Stent-induced vessel wall deformation

	Stent-induced Vessel Wall Deformation [mm]*										
Region	Successfully-treated						P	Partial η^2	SINE	P	Partial η^2
	cTAG	Valiant	Zenith	Ankura	Hercules	Grimed			-		
Entire region	3.305 (0.651)	3.962 (0.812)	3.149 (1.452)	3.735 (1.208)	2.843 (1.362)	2.934 (0.902)	.240	.130	5.309 (0.868)	.001	.184
Segment-1	2.779 (0.709)	1.849 (0.600)	2.389 (0.908)	2.794 (0.931)	2.235 (0.823)	2.232 (0.558)	.365	.106	3.632 (0.980)	.062	.063
Segment-2	3.715 (0.920)	2.444 (1.128)	3.700 (1.622)	4.371 (1.757)	3.418 (1.634)	3.851 (1.765)	.685	.062	5.295 (1.399)	.055	.066
Segment-3	3.385 (0.629)	2.345 (1.056)	3.713 (2.057)	4.257 (1.655)	2.915 (1.084)	3.223 (0.915)	.183	.144	6.702 (1.279)	.000	.224
Convex	3.405 (2.094)	3.464 (1.620)	4.052 (2.361)	4.492 (2.610)	3.265 (1.319)	3.555 (2.569)	.701	.060	4.305 (2.009)	.330	.018
Concave	4.641 (2.188)	3.649 (1.379)	3.727 (1.083)	4.452 (2.231)	3.986 (1.659)	3.887 (2.005)	.844	.041	4.959 (1.248)	.755	.002
Tear-side	3.969 (1.871)	2.992 (1.134)	4.340 (1.973)	4.074 (1.550)	3.269 (1.313)	3.663 (2.509)	.626	.081	4.427 (1.397)	.198	.031
Opposite Tear-side	4.076 (2.552)	4.121 (1.632)	3.440 (2.057)	4.871 (2.818)	3.982 (1.666)	3.779 (3.029)	.903	.041	4.837 (1.951)	.686	.165

* – The deformation data are presented as Mean (Standard Deviation).

Reference

1. Delingette H. General object reconstruction based on simplex meshes. Int J Comput Vision. 1999; 32: 111-46.

2. Montagnat J, Delingette H. 4D deformable models with temporal constraints: application to 4D cardiac image segmentation. Med Image Anal. 2005; 9: 87-100.

3. Larrabide I, Kim M, Augsburger L, Villa-Uriol MC, Rufenacht D, Frangi AF. Fast virtual deployment of self-expandable stents: method and in vitro evaluation for intracranial aneurysmal stenting. Med Image Anal. 2012; 16: 721-30.

4. Larrabide I, Radaelli A, Frangi A. Fast virtual stenting with deformable meshes: application to intracranial aneurysms. Med Image Comput Comput Assist Interv. 2008; 11: 790-7.

5. Vignon-Clementel IE, Figueroa CA, Jansen KE, Taylor CA. Outflow boundary conditions for three-dimensional finite element modeling of blood flow and pressure in arteries. Comput Method Appl M. 2006; 195: 3776-96.

6. Shang EK, Nathan DP, Fairman RM, Bavaria JE, Gorman RC, Gorman JH, 3rd, et al. Use of computational fluid dynamics studies in predicting aneurysmal degeneration of acute type B aortic dissections. J Vasc Surg. 2015; 62: 279-84.

7. Cheng Z, Wood NB, Gibbs RG, Xu XY. Geometric and flow features of type B aortic dissection: initial findings and comparison of medically treated and stented cases. Ann Biomed Eng. 2015; 43: 177-89.

8. Cheng Z, Riga C, Chan J, Hamady M, Wood NB, Cheshire NJW, et al. Initial findings and potential applicability of computational simulation of the aorta in acute type B dissection. J Vasc Surg. 2013; 57: 35s-43s.

9. Ballyk PD, Steinman DA, Ethier CR. Simulation of non-Newtonian blood flow in an end-to-side anastomosis. Biorheology. 1994; 31: 565-86.